Ahaliabadeh, Zahra; Miikkulainen, Ville; Mäntymäki, Miia; Colalongo, Mattia; Mousavihashemi, Seyedabolfazl; Yao, Lide; Jiang, Hua; Lahtinen, Jouko; Kankaanpää, Timo; Kallio, Tanja

Stabilized Nickel-Rich-Layered Oxide Electrodes for High-Performance Lithium-Ion Batteries

Published in:
Energy and Environmental Materials

DOI:
10.1002/eem2.12741

Published: 01/11/2024

Document Version
Publisher's PDF, also known as Version of record

Please cite the original version:
Ahaliabadeh, Z., Miikkulainen, V., Mäntymäki, M., Colalongo, M., Mousavihashemi, S., Yao, L., Jiang, H., Lahtinen, J., Kankaanpää, T., & Kallio, T. (2024). Stabilized Nickel-Rich-Layered Oxide Electrodes for High-Performance Lithium-Ion Batteries. *Energy and Environmental Materials*, *7*(6), Article e12741. https://doi.org/10.1002/eem2.12741

RESEARCH ARTICLE

Energy & Environmental Materials WILEY

Lithium-Ion Batteries

Stabilized Nickel-Rich-Layered Oxide Electrodes for High-Performance Lithium-Ion Batteries

*Zahra Ahaliabadeh, Ville Miikkulainen, Miia Mäntymäki, Mattia Colalongo, Seyedabolfazl Mousavihashemi, Lide Yao, Hua Jiang, Jouko Lahtinen, Timo Kankaanpää, and Tanja Kallio**

Next-generation Li-ion batteries are expected to exhibit superior energy and power density, along with extended cycle life. Ni-rich high-capacity layered nickel manganese cobalt oxide electrode materials (NMC) hold promise in achieving these objectives, despite facing challenges such as capacity fade due to various degradation modes. Crack formation within NMC-based cathode secondary particles, leading to parasitic reactions and the formation of inactive crystal structures, is a critical degradation mechanism. Mechanical and chemical degradation further deteriorate capacity and lifetime. To mitigate these issues, an artificial cathode electrolyte interphase can be applied to the active material before battery cycling. While atomic layer deposition (ALD) has been extensively explored for active material coatings, molecular layer deposition (MLD) offers a complementary approach. When combined with ALD, MLD enables the deposition of flexible hybrid coatings that can accommodate electrode material volume changes during battery operation. This study focuses on depositing TiO_2-titanium terephthalate thin films on a $LiNi_{0.8}Mn_{0.1}Co_{0.1}O_2$ electrode via ALD-MLD. The electrochemical evaluation demonstrates favorable lithium-ion kinetics and reduced electrolyte decomposition. Overall, the films deposited through ALD-MLD exhibit promising features as flexible and protective coatings for high-energy lithium-ion battery electrodes, offering potential contributions to the enhancement of advanced battery technologies and supporting the growth of the EV and stationary battery industries.

1. Introduction

$LiNi_{0.8}Mn_{0.1}Co_{0.1}O_2$ (NMC811) holds great promise as a next-generation lithium battery electrode material. However, the complex aging processes, including the formation of defective secondary NMC811 phases, have a profound impact on electrochemical performance resulting in progressive capacity fading. Thus, electrode aging remains a significant concern.[1–4] To extend the lifetime of lithium-ion batteries, a protective coating can be applied to the electrode surface to eliminate direct contact with the electrolyte species and protect against side reactions. Atomic layer deposition (ALD) has recently gained considerable interest as a technique for surface modification of Li-ion battery (LIB) electrodes. ALD employs self-limiting surface reactions to produce pinhole-free and conformal thin films on various substrates, including NMC811 electrodes.[5,6] Metal oxide coatings such as Al_2O_3, TiO_2, and ZrO_2 have been studied as a protection layer for battery electrode materials.[7,8] While coating NMC particles and electrodes with thin films can extend battery lifespan, they often hinder kinetics due to the poor lithium-ion conductivity of metal oxides, resulting in low initial capacity.[9] Moreover, the rigid metal oxide layer deposited through ALD cannot accommodate electrode volume change during cell cycling, which leads to cracking.[9–11]

In addressing these challenges, several studies have explored a versatile solution, that is the application of molecular layer deposition (MLD).[12–14] MLD is a technique that leverages organic materials for film deposition.[15] Recent studies have focused on the development of MLD films, including metallocenes, which are synthesized by combining metal-containing precursors and alcohols, as well as other hybrid organic/inorganic films.[12,13] Particularly, applying hybrid organic/inorganic films via MLD has garnered attention.[16] For example, Momtazi et al.[14] successfully grew a titanium carboxylate film using titanium tetraisopropoxide (TTIP) and succinic acid. Piper et al.[17] reported that the use of such aromatic organic precursors as hydroquinone (HQ) for MLD leads to a protective coating with improved mechanical strength and conductivity. Similarly, Vandenbroucke et al.[18] explored titanium carboxylate films deposited with tetrakis

---

Z. Ahaliabadeh, Dr. Asst. Prof. V. Miikkulainen, M. Colalongo,
Dr. S. Mousavihashemi, Dr. Prof. T. Kallio
Department of Chemistry and Materials Science (CMAT), School of Chemical Engineering, Aalto University, 02150, Espoo, Finland
E-mail: tanja.kallio@aalto.fi
Dr. M. Mäntymäki
Department of Chemistry, University of Helsinki, 00014, Helsinki, Finland
Dr. L. Yao, Dr. H. Jiang, Dr. J. Lahtinen
Department of Applied Physics, School of Science, Aalto University, 02150, Espoo, Finland
Dr. T. Kankaanpää
Umicore Finland Oy, 67101, Kokkola, Finland

The ORCID identification number(s) for the author(s) of this article can be found under https://doi.org/10.1002/eem2.12741.

DOI: 10.1002/eem2.12741

(dimethylamido)titanium and various dicarboxylic acid precursors, reporting enhanced lithium ion mobility, effective suppression of electrolyte decomposition at high voltages, and reduced irreversible electrochemical reactions. These MLD films exhibit remarkable flexibility, which plays a crucial role in mitigating structural deformation during prolonged cycling and ensuring stability for cathode materials. Moreover, the organic components present in these coatings contribute to the increased number of Li diffusion channels within the crystal structures, addressing the conductivity limitations typically associated with inorganic coatings.[18]

Building upon the promising findings of previous investigations, our present study focuses on synthesizing a novel material coating for NMC811 electrodes through the combination of ALD and MLD techniques. This unique approach enhances the structural and chemical stability of the coating, offering significant benefits for the protection of NMC811 electrodes during battery cycling. The ALD-MLD process involves the deposition of an organic–inorganic coating of TiO_2--titanium terephthalate on prefabricated NMC811 electrodes at a temperature of 200 °C. The coating is achieved by employing titanium (IV) isopropoxide, water, and terephthalic acid (TPA) as precursors. This novel organometallic coating on the NMC811 electrodes exhibits multiple advantages, including mitigation of electrolyte oxidation and reduction of electrode corrosion. Furthermore, it improves significantly the mechanical integrity of the NMC811 particles, stabilizes the interface between the NMC811 electrode and electrolyte, and effectively mitigates the irreversible structural phase transition of the NMC811 material. Consequently, the ALD-MLD coated sample exhibits highly controlled structural changes, demonstrating a remarkable 10-fold reduction in volume change compared to the uncoated sample. Notably, this innovative coating leads to enhanced capacity retention in the ALD-MLD coated NMC811 electrodes, retaining an impressive 85.7% of their initial capacity even after 500 cycles. In contrast, the uncoated NMC811 electrodes in a full-cell configuration only retain 56.2% of their initial capacity after the same number of cycles. This significant improvement is attributed to the flexibility conferred by the organic component of the coating, which substantially enhances Li diffusion and augments the initial cell capacity. Through this innovative approach, our research contributes to the development of a novel advanced artificial interphase for Ni-rich layer oxide electrode materials, opening new possibilities for the improvement of lithium-ion battery performance.

2. Results and Discussion

2.1. Structural Characterization

A common approach to increase the lifespan of high-voltage lithium battery positive electrode materials, such as NMC811, is to include additives in the electrolyte which form a cathode electrolyte interphase (CEI) during the first cycles.[19–21] The formed CEI comprises various inorganic and organic compounds and suppresses under the harsh operating environment detrimental further reactions between the active electrode material and electrolyte. Here we investigate as an alternative approach a flexible artificial CEI, a TPA-Ti film, directly coated on 1 mAh cm^{-2} NMC811 electrodes using the ALD-MLD technique. In this research, preliminary rate capability and cycling tests on NMC811 electrodes coated with TPA-Ti were performed to identify the ideal coating thickness and optimal TPA/Ti ratio. Different thicknesses and TPA/Ti ratios were investigated using various ALD-MLD cycles. As illustrated in Figure S2a, Supporting Information, deviating from the ratio of 1/12 did not enhance the specific capacity; instead, it resulted in a decrease, particularly evident at higher C-rates. Notably, the NMC-TPA-Ti sample with the TPA/Ti ratio of 1/12 and a thickness of 8 nm exhibits the specific discharge capacity across various C-rates, as depicted in Figure S2, Supporting Information. It is imperative to acknowledge that altering the ALD-MLD ratio directly influences the coating thickness. Increasing the ALD/MLD ratio reduces the coating thickness, while decreasing it, leads to a thicker coating. Consequently, a ratio of 1/12 demonstrated the optimal balance, resulting in superior capacity, and thus was selected as the ideal ratio for subsequent experimental analyses.

Based on these promising results, this optimized sample is selected for further characterization and electrochemical performance evaluations. The effect of the TPA-Ti coating on the crystal structure of the NMC811 electrodes was investigated by XRD experiments. Figure S4, Supporting Information shows the XRD patterns of NMC-ref and NMC-TPA-Ti and no impurity phases nor diffraction peaks from the coating are visible, which is ascribed to the amorphous nature of the coatings or their nanoscale thicknesses.[22] Next characterization analysis focuses on the morphology of the optimal sample (NMC-TPA-Ti) using scanning electron microscopy (SEM) imaging (**Figure 1**a,b). This analysis reveals that the morphology of the NMC-TPA-Ti electrode closely resembles that of the pristine NMC-ref electrode. The SEM images reveal a consistent particle structure with no significant differences observed on the surface of the secondary particles. Elemental mapping of Ni (Figure 1c,e), as well as Mn and Co (Figure S3, Supporting Information), confirm the uniform distribution of the transition metals (TM) in both the NMC-ref and NMC-TPA-Ti electrodes. Importantly, the surface of the NMC-TPA-Ti electrode displays a clear presence of Ti covering the entire electrode surface. In contrast, energy-dispersive X-ray spectrometer (EDS) yields a noisy and inconclusive scattering pattern of Ti on the NMC-ref electrode indicating that no Ti is detected. These findings demonstrate the successful deposition of the Ti-containing film on the NMC811 electrode surface, providing insights into the elemental distribution and the enhanced surface composition achieved through the ALD-MLD coating process.

To gain deeper insights into the evolution of the TPA-Ti coating within the NMC811 structure, a cross-sectional high-resolution transmission electron microscopy (TEM) study was conducted. The preparation of TEM lamella samples, as described in our previous work,[22] involved utilizing the focused-ion beam-SEM (FIB-SEM) techniques. In this process, a platinum (Pt) strap was deposited on the NMC811 surface, acting as a protective layer for the specimen, as shown by the black dotted line in **Figure 2**a. The TEM analysis focused on a specific region of interest, as highlighted by the blue box in Figure 2a. The electron microscopy analysis provides valuable insights into the TPA-Ti coating on the NMC811 particles. Figure 2b illustrates an NMC811 particle with an approximate TPA-Ti thickness of 8 nm, displaying a consistent and uniform surface coating. To verify the uniformity of this coating, additional TEM analysis was performed on a randomly selected second lamella sample, as depicted in Figure S5, Supporting Information. The results from Figure 2 and Figure S5, Supporting Information collectively demonstrate that the coating layer uniformly covers the electrode surface, with a thickness consistently measuring around 8 nm across all samples. Furthermore, X-ray EDS elemental mappings were conducted on selected areas of the electrode sample, as illustrated in Figure 2c,d. These mappings reveal the successful incorporation of Ti

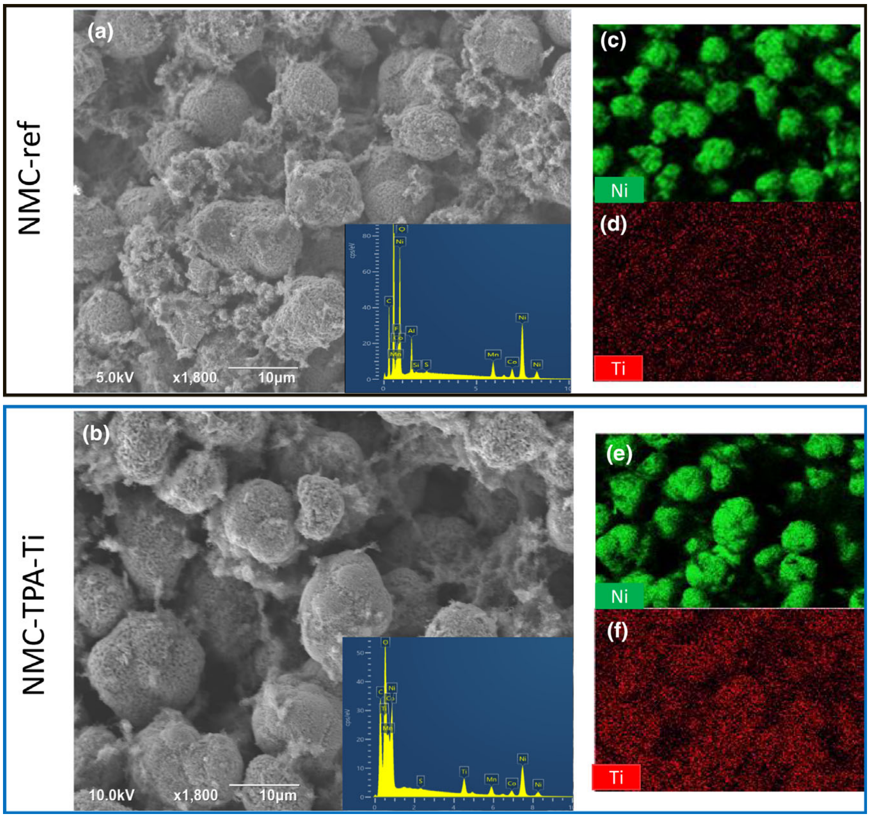

Figure 1. A SEM image and corresponding EDS spectra/mapping for the NMC-ref and NMC-TPA-Ti samples.

into the grain boundaries (GBs) of the NMC811 particles. This effective combination of surface coating and GB engineering has a significant impact on enhancing cycling stability by minimizing the occurrence of intergranular cracks.[22–25] These findings underscore the high potential of the TPA-Ti coating in improving the structural integrity of NMC811 electrodes, ultimately leading to enhanced performance and durability.

As neither SEM-EDS nor TEM-EDS yields information on the actual hybrid TPA-Ti formation, Fourier transform infrared spectroscopy (FTIR) analysis was performed to investigate the chemical bonds present in the coatings, shedding light on the organic part of the coating and surface characteristics. **Figure 3** showcases the as-deposited coating layer on the NMC811 electrode surface, while Figure S6, Supporting Information presents supplementary FTIR results obtained from the TPA-Ti-Si wafer. Upon comparison of the bare and TPA-Ti coated Si wafer (Figure S6, Supporting Information), the most prominent features are observed within the range of 1600–1400 cm^{-1}, which can be attributed to the asymmetric and symmetric vibrations of the benzene ring and carboxylate anion in the coating.[18,26] Specifically, in the TPA-Ti-Si sample, the peaks at 1571 and 1510 cm^{-1} showcase the asymmetric (ν_{as}) and symmetric (ν_s) stretching bands of the carboxylate anion (COO^-), respectively.[26,27]

Moving to the FTIR results for the coated electrode (Figure 3), two series of data are obtained. The FTIR analysis of the thin film (8 nm) coated NMC811 does not clearly reveal the presence of the coating layer chemical bonds on the electrode surface, which can be attributed to the nanoscale thickness of the coating and the limited surface sensitivity of FTIR in this context. However, when the TPA-Ti thickness is increased five-fold, the peaks at 1571 and 1510 cm^{-1} in the FTIR spectrum are detected, showing expectedly the carboxylate anion (COO^-) asymmetric (ν_{as}) and symmetric (ν_s) stretching bands, respectively.[27,28] Additionally, a broad peak at 940 cm^{-1} corresponding to O-H is observed, which may be attributed to unreacted terephthalic acid molecules or absorbed water molecules from exposure to the ambient atmosphere.[18,29] The band at 826 cm^{-1} is associated with the =C–H bending of an aromatic ring.[26] Furthermore, a peak in the low-frequency range of 500–800 cm^{-1}, shows the presence of Ti-O-Ti bonds.[18,29] However, it should be noted that identifying Ti-O-Ti in the coated electrode FTIR analysis alone is challenging due to the presence of several components in the electrode composite, which may result in overlapping peaks. Therefore, further insights into the surface properties are provided through X-ray photoelectron spectroscopy (XPS) analysis, as discussed in the subsequent paragraph.

XPS measurements were performed on the NMC-ref and NMC-TPA-Ti electrodes, and the resulting data are presented in **Figure 4**. The O 1s spectra (Figure 4a) exhibit distinct components, including one at a

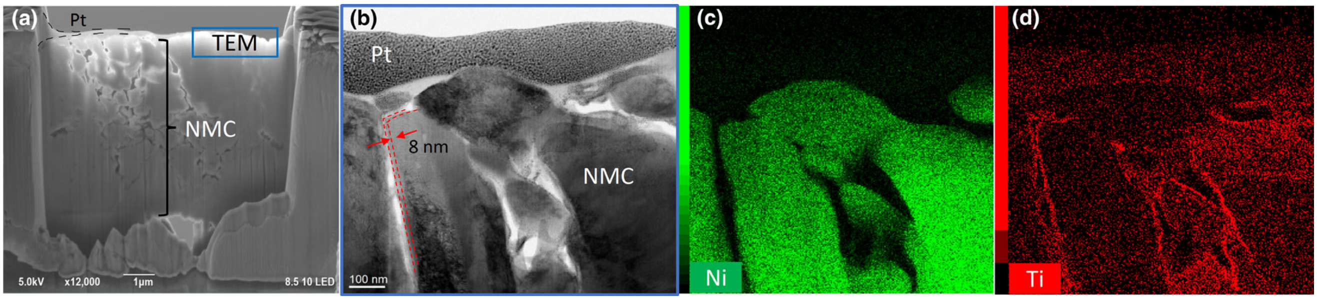

Figure 2. a) A FIB/SEM image of a lamella containing the NMC-TPA-Ti covered by a Pt film, b) STEM bright-field images of NMC-TPA-Ti and representative EDS mapping for the c) Ni and d) Ti elements.

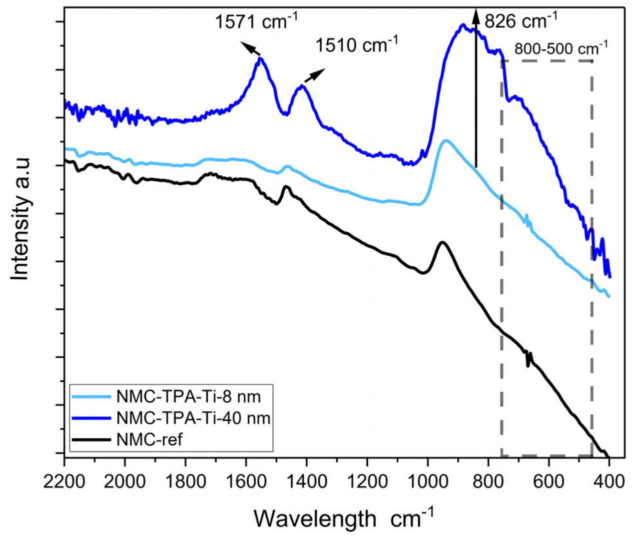

Figure 3. FTIR results for NMC-ref and NMC-TPA-Ti with different thicknesses of 8 and 40 nm.

low energy level 529.2 eV (TM-O) corresponding to oxygen bonded to the transition metals.[30] The binding energy of another component at 531.0 eV can be attributed to the carboxylate ion present in the coating.[18] This component is more prominent in the NMC-TPA-Ti electrode.[31] The large peak between 531 and 532 eV is due to carbonyl or carboxylate groups from Li_2CO_3 on the surface of both coated and uncoated electrodes. There is also a shoulder representing C–O bonds (534.0 eV) due to exposure to ambient air.[18,22,32] In the C 1s spectra (Figure 4b), multiple components are observed for both the NMC-ref and NMC-TPA-Ti electrodes. These components include C–C/C-H bonds (284.4 eV) serving as a calibration reference,[33] and C–O bonds (286.5 eV) originating from air exposure. The presence of an organic compound within the deposited film is suggested by the higher C–O intensity in the NMC-TPA-Ti electrode.[18,34,35] Additionally, a low concentration of Li_2CO_3 surface impurity is detected, likely resulting from air exposure during sample storage, leading to C=O bonding (288.8 eV) in both samples.[32] Because the carbon concentration on the surface is much higher than that of oxygen, the main component (C=O) in the O1s spectra corresponds to only a tiny peak in C 1s. The Ti spectra (Figure 4c) show the Ti 2p doublet with the peak positions and shape typical to TiO_2.[22] These findings from XPS analysis are consistent with the FTIR results, providing further evidence for the formation of a TiO_2-titanium terephthalate film on the NMC811 surface.

2.2. Electrochemical Characterization

After showcasing the successful deposition of the aspired organometallic coating, the optimized sample was subjected to evaluation of electrochemical performance. In particular, the rate capability and the cycling performance of the coated NMC-TPA-Ti electrodes were investigated and compared to the NMC-ref electrode to investigate the artificial CEI effect on the electrode functionality. The rate capability curves of the NMC-ref and NMC-TPA-Ti electrodes were obtained by subjecting half cells to charge/discharge cycles at various C-rates (0.1, 0.2, 0.5, 1, 2, 4, and 5 C) within the voltage range of 3.0–4.4 V (**Figure** 5a). The rate capabilities of the NMC-TPA-Ti electrode are consistently higher than those of the NMC-ref electrode at the different C-rates, except for 4 and 5 C, indicating that the coating does not significantly hinder the diffusion of Li^+ ions at low C-rates.[22,36] However, the impact of the coating on the capacity, attributed to increased kinetic limitations, becomes more pronounced at the higher C-rates. Phattharasupakun et al.[37] revealed that cycling at high rates, where Li-ion (de)intercalation primarily occurs on the surface, leads to reduced Li-ion kinetics and limited accessible capacity during subsequent cycle. The presence of a coating on the surface can further impede Li-ion mobility, especially when it covers both the surface and grain boundaries.[22] To illustrate this, we compare the galvanostatic charge–discharge profiles of the first cycle at 0.1 C in Figure 5b. The results show that NMC-TPA-Ti exhibits a higher coulombic efficiency compared to the uncoated sample, indicating that the presence of the coating protects against side reactions and lithium loss. At these low C-rates, neither kinetic nor mass transfer limits the performance as comparable discharge capacities with the NMC-ref electrode are obtained. This observation together with the rate capability results confirm that the presence of the coating does not compromise discharge capacity at low C-rates. The higher capacity loss in the NMC-ref electrode at the low C-rates can be attributed to detrimental side reactions that occur at high cut-off voltages, leading to Li loss and capacity decay.[38,39]

Metal oxides[40] and metal phosphates,[41] have been studied as protective layers on the surface of Ni-rich cathode materials, but their low ionic conductivity limits the initial discharge capacity. In contrast, the TPA-Ti coating provides higher capacity for NMC811 at different C-rates and enhanced stability as evidenced by the higher capacity retention at the final 0.2 C cycling step, as shown in Figure 5a. The TPA-Ti coated NMC811 electrodes exhibit enhanced capacity retention, with 100% retention compared to 96% for the NMC-ref electrode. This indicates a more reversible capacity for NMC-TPA-Ti enhancing the available energy density for practical applications. Furthermore, the significant improvement enabled by the TPA-Ti coating is further confirmed in the long-term cycling results at 1 C ($1\ C = 200\ mA\ g^{-1}$) for 100 cycles within the voltage range of 3.0–4.4 V in the half-cell setup. As shown in Figure 5c, the capacity retention is 97% for TPA-Ti-NMC and 88% for NMC-ref after 100 cycles, highlighting the positive influence of the TPA-Ti coating on cycling stability and capacity retention. Extending the cycling study to 180 cycles indicates that the TPA-Ti coating enables significant improvement, as shown in Figure 5c, where the capacity retention is 91% and 80% for TPA-Ti-NMC and NMC, respectively. It is worth noting that the unique structure of the coating, as elucidated in the study by Philip et al.,[15] plays a pivotal role in improving electrode performance and evidently stabilizes the CEI. The mechanism behind the beneficial effect of the TPA-Ti coating on the NMC811 electrode during cycling is further analyzed through cyclic voltammetry (CV), electrochemical impedance spectroscopy (EIS), and dilatometry. These analyses reveal factors behind the improved performance of the TPA-Ti coated electrode by yielding information on Li^+ ions transfer and kinetics as well as mechanical strength and volumetric changes of the electrode.

Figure 6a,b depict the CV curves of the NMC-ref and NMC-TPA-Ti electrodes, measured between 3.0 and 4.4 V vs Li/Li^+ at various scan rates (0.02, 0.1, 0.2, and $0.5\ mV\ s^{-1}$). Upon cycling at these scan rates, the electrode reversibility is evaluated by reverting the scan rate to $0.02\ mV\ s^{-1}$ (Figure S7, Supporting Information). At first sight, the CV curves reveal that the presence of the TPA-Ti coating does not significantly alter the primary electrochemical reaction kinetics compared to

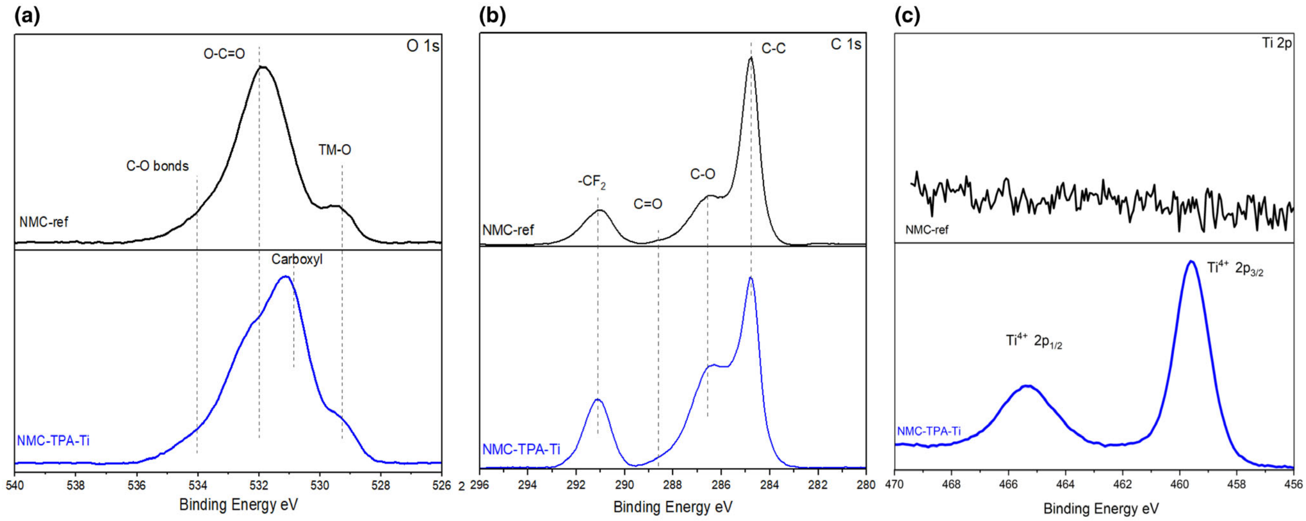

Figure 4. XPS of NMC-ref and NMC-TPA-Ti: a) O 1s spectra, b) C 1s spectra, and c) Ti 2p spectra.

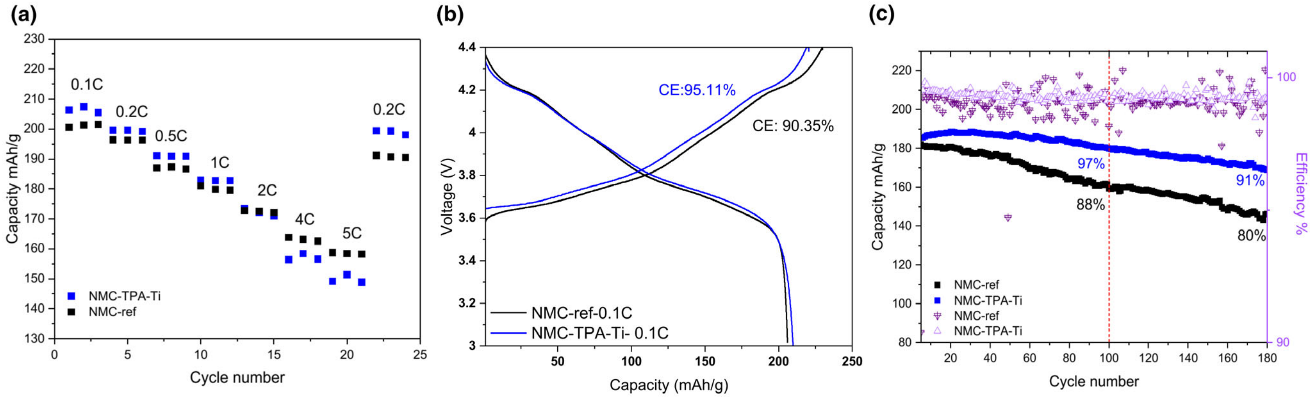

Figure 5. Electrochemical performance of the NMC-ref and NMC-TPA-Ti electrodes in half cells. a) The rate capability of the electrodes at various current densities in a voltage range of 3.0–4.4 V. b) Galvanostatic charge–discharge at initial cycles of 0.1 C. c) Long-term cyclability (charged and discharged at 1 C) of the electrodes in the voltage range of 3.0–4.4 V.

the NMC-ref electrode which is in agreement with the rate capability results. NMC-ref and NMC-TPA-Ti demonstrate distinct pairs of anodic/cathodic peaks denoted as H1-H2 and H2-H3, indicating the multiphase transition within the Ni-rich layered oxide cathode material. The distinct cathodic/anodic peaks for NMC-ref are detected at H1-H2 = 3.75 V and H2-H3 = 4.24 V, while for NMC-TPA-Ti, they are observed at H1-H2 = 3.77 V and H2-H3 = 4.24 V, at a scan rate of 0.1 mV s^{-1}.[42,43] With the increasing scan rates, the strongest oxidation peak of the NMC-ref electrode experiences a more substantial shift toward more positive potential compared to the NMC-TPA-Ti electrode. As such, for each cycle at the scan rates of 0.1, 0.2, and 0.5 mV s^{-1}, the NMC-ref electrode exhibits potential shifts of 0.05, 0.16, and 0.36 V, respectively, while the NMC-TPA-Ti electrode demonstrates shifts of 0.03, 0.12, and 0.25 V, respectively.

Moreover, upon returning to the scan rate of 0.02 mV s^{-1}, the anodic/cathodic peaks show a bigger shift for the NMC-ref electrode, whereas the NMC-TPA-Ti electrode exhibits enhanced reversibility (Figure S8, Supporting Information). This observation indicates mitigation of electrochemical polarization and an improvement in electrochemical reversibility due to the integrated modification provided by the TPA-Ti coating.[29,44] These findings support the TPA-Ti coating positive contribution to improved electrochemical performance and stability, consistent with the previously discussed rate capability and long-term cycling results.

To further study the degradation mechanism, detailed information about the CEI is obtained by conducting EIS measurements. **Figure 7** displays the Nyquist plots of the NMC-ref and NMC-TPA-Ti electrodes, both at the 1st cycle (following the formation cycle) and the 50th cycle. The equivalent circuit embedded in the figures represents the fitted impedance spectra, and the corresponding resistance values can be found in Figure S7, Supporting Information. The equivalent circuit consists of various components contributing to the impedance spectra. R_S represents the ohmic resistance, R_{CEI} relates to the diffusion resistance of Li^+ through the CEI layer, R_{GB} reflects the grain boundary resistance, and R_{CT} represents the charge-transfer resistance, which characterizes the overall impedance of the lithium-ion battery.[44,45]

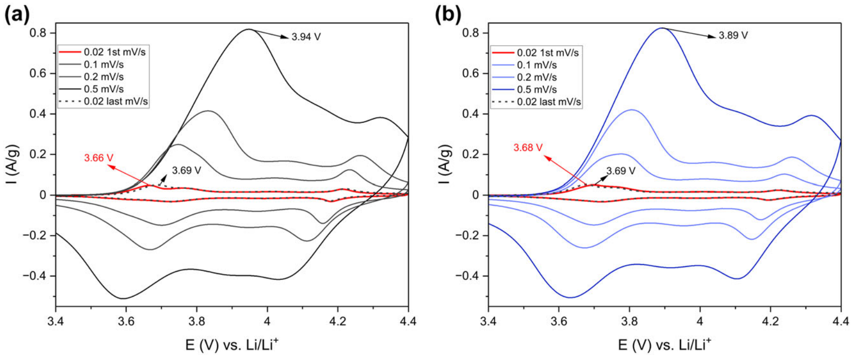

Figure 6. Cyclic voltammograms measured in the three-electrode setup for a) the NMC-ref and b) NMC-TPA-Ti samples at different scan rates of 0.02, 0.1, 0.2 and 0.5 mV s^{-1}.

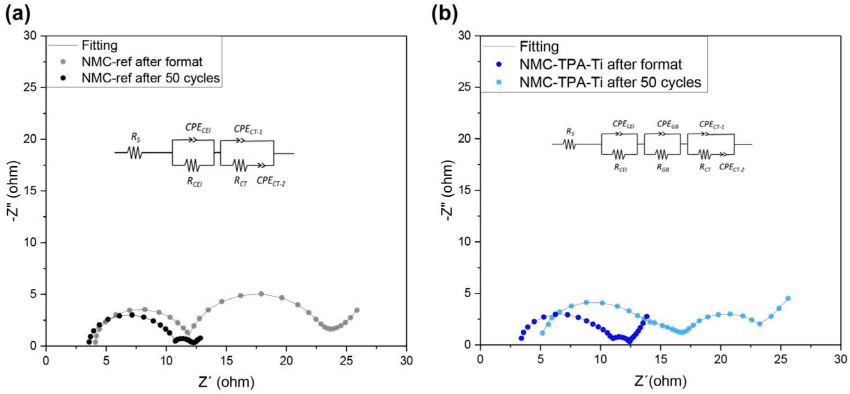

Figure 7. Nyquist plots of a) NMC-ref and b) NMC-TPA-Ti at 1st cycle and 50th cycle in a half-cell configuration—all measurements were done in the three-electrode setup at room temperature and SOC 50%.

In TEM analysis (Figure 2), the presence of both surface and grain boundary coating is successfully demonstrated. Upon analyzing Figure 7a,b, it becomes clear that NMC-TPA-Ti demonstrates similar R_{CEI} compared to NMC-ref. This similarity can be attributed to the fact that the EIS measurements were conducted at SOC 50% where the electrochemical behavior (Figure 5b) is nearly identical for both samples. However, in the coated sample, a second semicircle is discernible. It is identified as R_{GB}, which is due to an additional diffusion barrier resulting from the TPA-Ti coating within the grain boundaries. The TPA-Ti surface coating on the NMC811 electrode acts as a barrier for the mobility of Li$^+$ ions, as explained in a previous research.[46] The presence of R_{GB} impedance contributes to the observed lower rate capability at higher C-rates of 4 and 5 C by creating a concentration gradient of Li$^+$ ions between the electrode surface and the bulk, thereby affecting Li transfer.[46,47]

As the number of cycles reaches 50, both NMC-ref and NMC-TPA-Ti demonstrate an increase in resistance for R_{CEI} and R_{GB}. This phenomenon can be attributed to anisotropic volume changes, which lead to intergranular cracking of the secondary particles. Such cracking creates new sites for CEI layer growth and the accumulation of byproducts resulting from the electrolyte decomposition. Therefore, the primary cause of the rise in resistance is the occurrence of reactions at the electrode-electrolyte interface. The conductivity of the CEI layer can be influenced by various reactions occurring at the surfaces of both coated and uncoated electrodes. The growth of the CEI on the electrode surface impedes the mobility of Li$^+$ ions due to its poor ionic conductivity, consequently, increasing cell impedance, as described in previous studies.[6,22] To assess the impact of differences in the CEI layer growth on the coated and uncoated samples, the charge-transfer resistance (R_{CT}) is of paramount importance. In NMC-ref, the R_{CT} values show a significant increase during 50 cycles, reaching 12.5 Ω. In contrast, NMC-TPA-Ti demonstrates a more moderate increase, reaching 8.3 Ω over the same duration. The lower resistance observed in NMC-TPA-Ti can be attributed to the improved ionic conductivity of the electrode resulting from the surface modification, as previously reported.[48] These findings align with our long-term cycling results, showing that the coated sample maintains higher capacity retention due to the stabilized structure of the CEI interphases.

Analyzing the performance of the coated electrodes in a full-cell setup is crucial for their commercialization.[49] Constructing full cells with graphite allows for the evaluation of the stabilizing effect of the TPA-Ti coating while avoiding any detrimental interactions between the electrolyte and Li metal counter electrode.[50] **Figure 8** presents a comparison of the long-term cycling performance between NMC-ref and NMC-TPA-Ti in a full-cell configuration at 1 C. Similar to the half-cell results, the full-cell also demonstrates superior cycling stability with excellent coulombic efficiencies. The stability test of the full cells is conducted for 500 cycles, with the corresponding voltage range of 2.9–4.3 V. NMC-TPA-Ti exhibits higher capacity retention of 92% after 300 cycles and maintains its state of health (SOH) above 80% even after 500 cycles, showing almost constant discharge voltage after 500 cycles. On the contrary, NMC-ref reaches 80% SOH just after 150 cycles while after 300 cycles the capacity retention is only at 66%. After 500 cycles, NMC-ref has experienced notable degradation as its capacity retention has decreased to 56%, which is significantly lower compared to NMC-TPA-Ti. In line with the half-cell cycling results (Figure 5), the electrodes initially deliver comparable specific discharge capacity, NMC-ref 178 mAh g^{-1} and NMC-TPA-Ti 176 mAh/g. The lower initial specific discharge capacity (lower coulombic efficiency) observed in the full cells, compared to the half-cells in Figure 5, is primarily attributed to the consumption of active lithium during the formation of the solid electrolyte interphase (SEI) on the anode.[50,51] However, the initial capacities remain comparable between NMC-ref and NMC-TPA-Ti in the full-cell configuration.

2.3. Postmortem Analysis

To gain deeper insights into the morphological and structural changes of the NMC-ref and TPA-Ti-NMC electrodes, a comprehensive postmortem analysis was conducted using SEM and tomography. For the

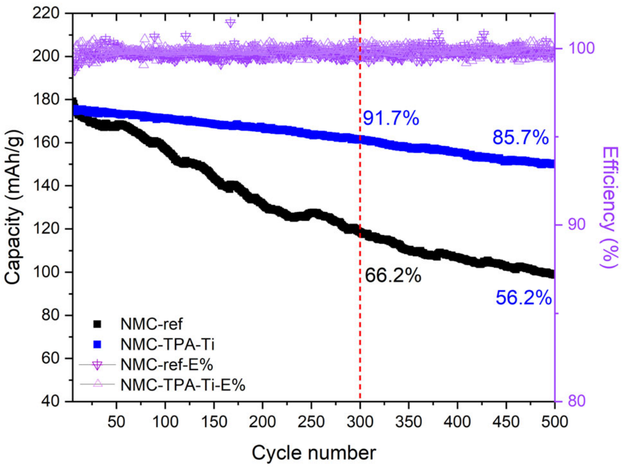

Figure 8. Long-term cyclability (charged and discharged at 1 C) of NMC-ref and NMC-TPA-Ti in the voltage range of 2.9–4.3 V versus graphite.

postmortem SEM, the aged samples were subjected to 180 cycles in the half-cell and 500 cycles in the full-cell configuration. The SEM analysis of the cycled NMC-ref particles (as depicted in **Figure 9**a) unveils the presence of surface cracks in both the half-cell and full-cell configurations, indicating structural degradation. In contrast, the NMC-TPA-Ti sample exhibits remarkable stability throughout the entire cycling process. These findings highlight the reduced occurrence of surface cracks in the NMC-TPA-Ti electrode, which can be attributed to the advantageous mechanical protection provided by the TPA-Ti as a flexible coating.[52]

The morphology of the NMC-ref and NMC-TPA-Ti samples after 20 and 50 aging cycles was investigated using X-ray tomography, providing valuable insights into crack generation and porosity development. Figure S9, Supporting Information displays 2D cross-sections of the samples.[53] To achieve high 3D resolution, tomography imaging was employed, enabling the visualization of sub-particle defects and crack propagation as a function of cycle number.[54] **Figure 10**a,b presents 3D renderings of the NMC-ref and NMC-TPA-Ti electrodes clearly visualizing the secondary particles after cycling, offering a clear view of their internal morphology.

In Figure S11, Supporting Information, a 3 dimensions (3D) rendering of the fresh NMC-ref after the formation cycle serves as a benchmark, showing no clear crack formation but revealing a few instances of central porosity and voids originating from the secondary particles before cycling. After the calendering process, both electrodes initially exhibit cracks, as a result of the calendering. However, the subsequently deposited artificial CEI effectively conceals these early-stage cracks and grain boundaries, as evident in the TEM images (Figure 2). Consequently, Figure 10b shows that in the coated sample the NMC811 particles near

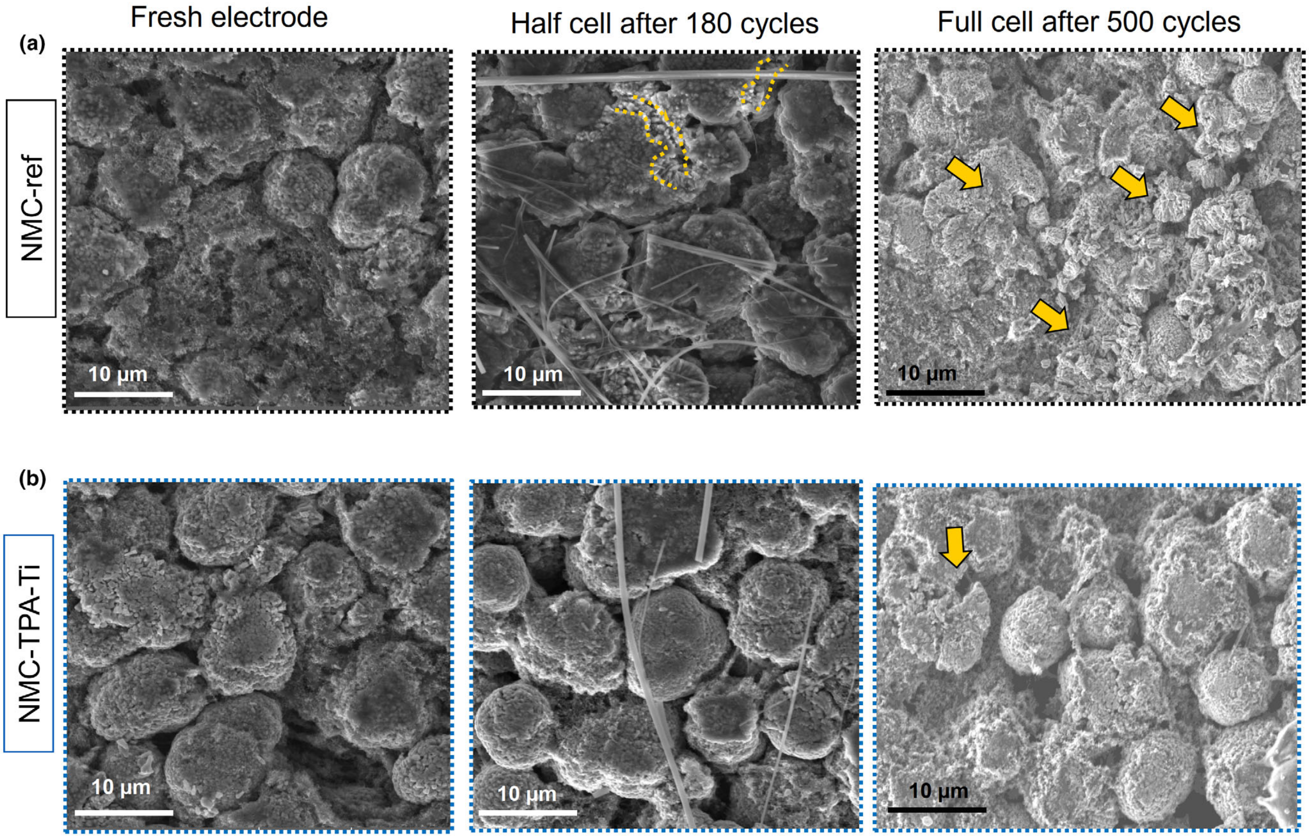

Figure 9. SEM images of a) fresh NMC-ref (left-handed side upper row) and b) NMC-TPA-Ti (left-handed side lower row) and postmortem of NMC-ref and NMC-TPA-Ti aged for 180 cycles (middle) and 500 cycles (right-hand side) in the half-cell and full-cell configurations, respectively.

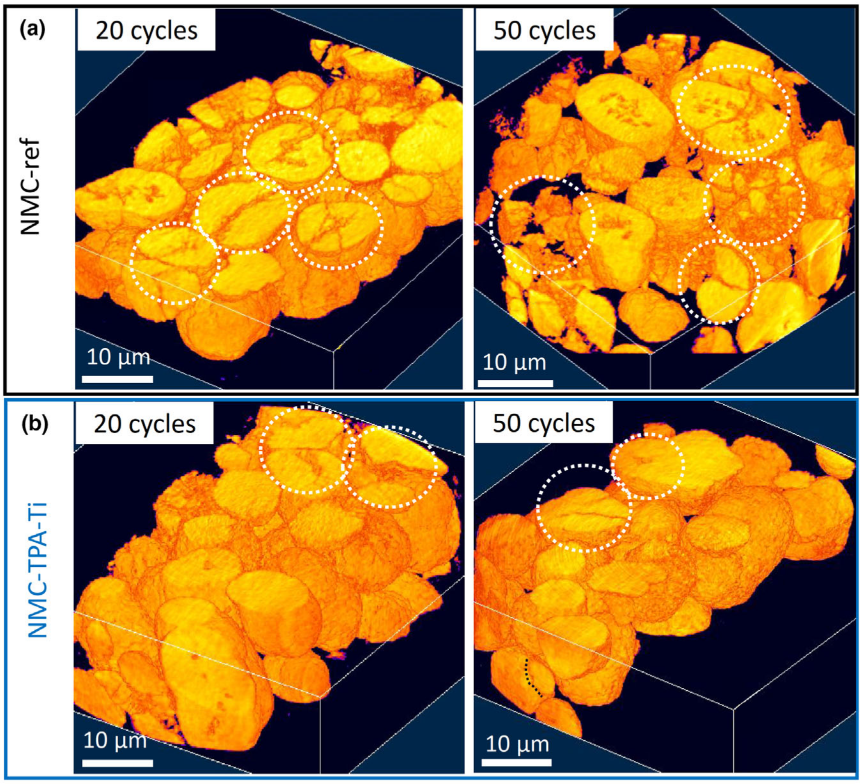

Figure 10. Visualization of the 3D reconstruction images of the a) NMC-ref and b) NMC-TPA-Ti after (left) 20 cycles and (right) 50 cycles of charge and discharge in the half-cell configurations, using the volume view plugin, in ImageJ.

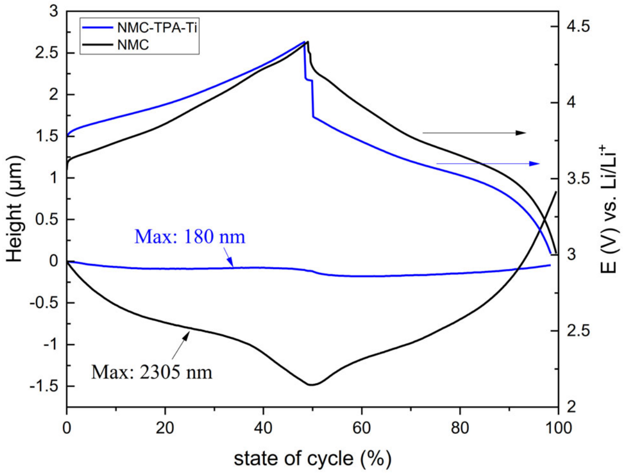

Figure 11. NMC-ref and NMC-TPA-Ti electrode height change and charge–discharge potential versus Li/Li^+ at 0.1 C as a function of the experimental state of the cycle where 0 and 50% correspond to fully charged and discharged cells, respectively.

the surface experience less degradation during the cycling, consistent with the electrochemical findings from the long-term cycling. In both the NMC-ref and NMC-TPA-Ti samples, porosities and cavities are observed within the secondary particles of the charged electrodes. However, a noticeable difference is evident from Figure 10a, where the NMC-ref sample exhibits a higher porosity, which increases as the cycle number reaches 50. This higher porosity contributes to the formation of low-density regions surrounding the microcracks within the secondary particles.[55,56]

Observations of intergranular microcrack generation and propagation along grain boundaries in both the NMC-ref and NMC-TPA-Ti samples align with the above postmortem SEM analyses. These microcracks result from the release of internal mechanical stress accumulated during charging and discharging, attributed to the accumulation of structural, chemical, and charge heterogeneities within the electrode.[57–59] Notably, the 50-cycles aged NMC-ref sample exhibits a higher number of cracks compared to the corresponding NMC-TPA-Ti electrode. Moreover, the propagation of the cracks results in the smashing of the secondary particles, as indicated by the white dotted circles in the tomography images (Figure 10). These findings are consistent with the long-term cycling data, emphasizing that crack formation exposes more particle surface to the electrolyte. The reduced occurrence of cracks in the NMC-TPA-Ti electrode suggests lower volume change during cycling, which is further examined below using operando X-ray diffraction analysis (XRD) and dilatometry analysis. Additionally, the presence of an overlaying artificial CEI on the particle surface helps to alleviate detrimental side reactions, thus preserving long-term cycling stability.[25]

2.4. Operando Dilatometry and XRD Analysis

Volume changes during charge and discharge, resulting from Li (de) intercalation, induce mechanical stress and strain in NMC811 active materials. This significant detrimental side effect is associated with the mechanical fracture and crack formation of the electrode materials. To gain a comprehensive understanding of the volume change behavior in the NMC-ref and NMC-TPA-Ti electrodes, operando dilatometry and XRD experiments were conducted during galvanostatic charge and discharge processes in the voltage range of 3.0–4.4 V versus Li/Li^+.

In order to ensure accurate measurements both the NMC-ref and NMC-TPA-Ti samples were meticulously prepared and studied under standardized conditions. Initial findings of the dilatometry analysis, depicted in **Figure 11**, illustrate that both the NMC-TPA-Ti and NMC-ref electrodes exhibit structural expansion during charging, attributed to the increase in the *c*-lattice parameter up to 4.2 V. Subsequently, a sudden volume shrinkage occurs due to the extraction of Li from the NMC811 structure.[22,30] The magnitude of this shrinkage is notably lower for NMC-TPA-Ti which highlights the importance of the coating in controlling volume variations during charging and minimizing the risk of mechanical fracture.

Recently, a study conducted by Spingler et al.[60] has focused on investigating the changes in NMC811 electrode thickness using dilatometry. Their analysis reveals a strong correlation between the magnitude of height changes and variations in the *c*-axis length, particularly during the charging process. They observed that the height change is primarily influenced by factors such as the expansion of active material particles within the electrode structure, the non-preferential orientation of grains, and changes in porosity. These factors contribute to the height change during the discharge process and prevent the electrode height from returning to its initial structure. By considering the insights provided by Spingler et al., it becomes evident that the height variations in the NMC811 electrode are closely tied to the structural dynamics occurring during charge. Building upon these insights, our dilatometry results in Figure 11 corroborate the effectiveness of the TPA-Ti coating in mitigating the NMC811 electrode height changes, particularly at high cut-off voltages, in agreement with observations for coatings in prior studies.[22,60,61] Importantly, as shown in Figure 11, the maximum height reached is more than 20 times higher (2305 nm) compared to NMC-TPA-Ti (180 nm). Moreover, notably larger irreversible height change is demonstrated by NMC-ref (840 nm) when compared to NMC-TPA-Ti (46 nm). The lower overall height change and higher reversibility observed in NMC-TPA-Ti indicate that the coating restricts thickness changes. The application of the TPA-Ti coating plays a vital role in significantly improving cycling stability as clearly demonstrated by the notable capacity retention enhancements during the long-term cycling (Figures 5 and 8). This appears to be related to reducing electrode volume changes, and in crystal lattice level to *c*-axis contraction.[22,60]

Hu et al.[11] previously suggested that irreversible, anisotropic, and mesoscale expansion/shrinkage of nano-grains during the cycling can be the primary driving force for microcrack initiation at the grain boundaries. This is confirmed by operando XRD measurements supporting the presence of irreversible lattice and morphological changes that induce microcracks. Therefore, the flexible and protective nature of the coating plays a crucial role in maintaining the structural integrity of the electrode. Our post-mortem analysis, showing improved mechanical integrity (Figure 9), further supports this. Thus, our results demonstrate a correlation between higher stability, reduced mechanical deformations, and minimized undesired volume changes in the electrode, all enabled by the flexible and protective NMC-TPA-Ti coating.

In addition to analyzing the electrode height changes through dilatometry, operando XRD analysis was employed to examine the alterations in the lattice parameters during the (de)lithiation process of the NMC811 electrode. To achieve this, XRD measurements were conducted on an NMC811/Li half-cell during its initial electrochemical cycle, in a voltage range from 3.0 to 4.4 V. Contour plots presented in **Figure 12** illustrate the XRD patterns at specific 2theta

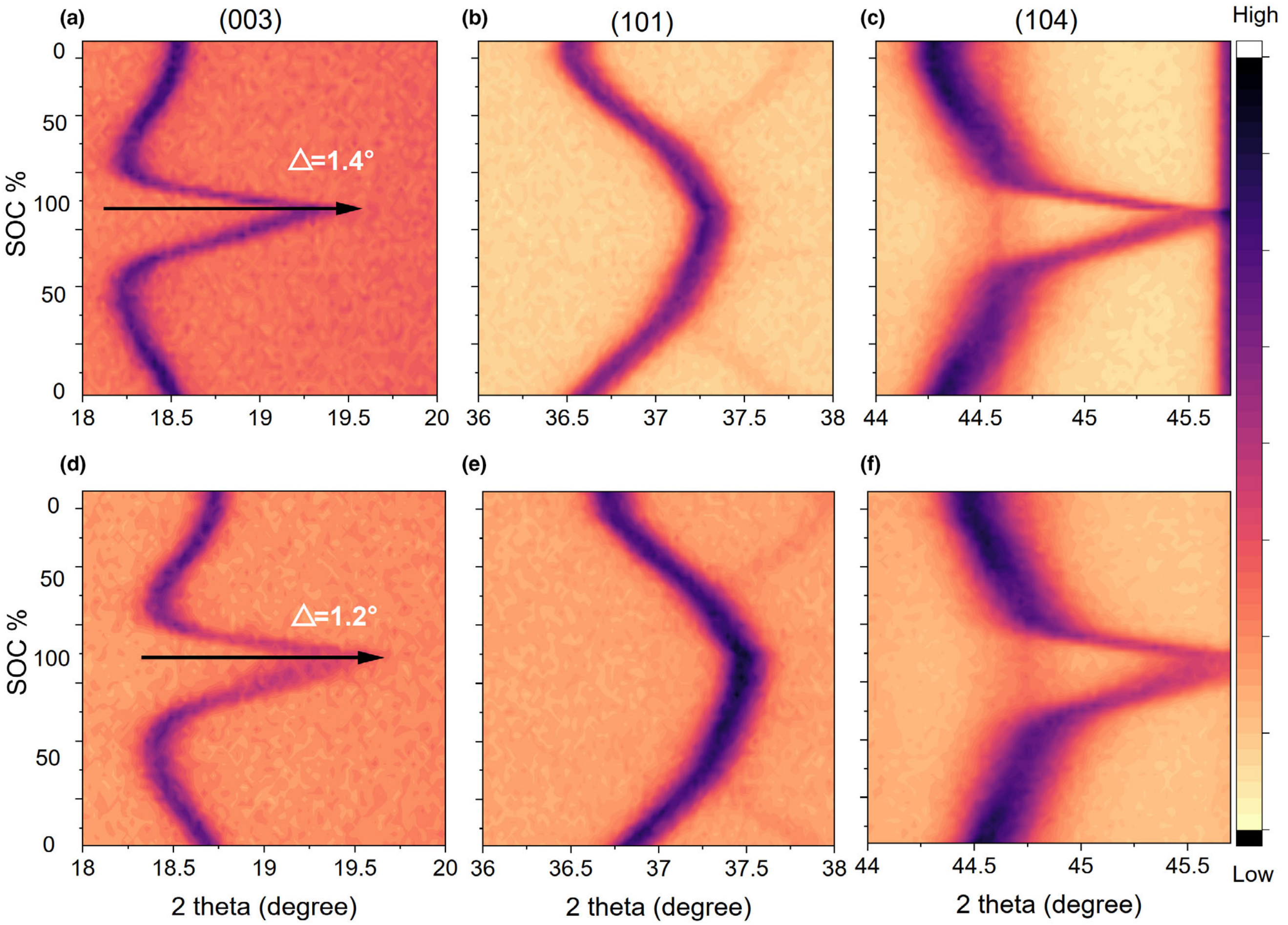

Figure 12. Operando XRD results: Contour plots showing three selected 2theta regions of the XRD pattern for both a–c) NMC-ref and d–f) NMC-TPA-Ti during initial cycling at 0.1 C in 3.0–4.4 V versus Li/Li$^+$.

regions corresponding to the (003), (101), and (104) crystallographic planes.

Typically, during charging in NMC-based materials, the (003) peak shifts toward lower angles associated with an increase in the *c* parameter, while the (101) and (104) peaks shift toward higher scattering angles indicating a contraction in the lattice *a* axis. This behavior is attributed to the increased electrostatic repulsion between adjacent transition metal layers within the NMC811 structure associated with the oxidation of $Ni^{2+/3+}$ ions and lithium deintercalation.[60,62] At the end of the charging process, the (003) reflection rapidly shifts toward higher angles, signifying the oxidation of $Ni^{2+/3+}$ ions to smaller Ni^{4+} ions, as shown in Figure 12. This transition results from the deintercalation of a critical amount of lithium, leading to a decrease in electrostatic repulsion between transition metal layers and inducing a rapid lattice shrinkage at high cut-off voltages (4.2–4.4 V).[63]

While both the NMC-TPA-Ti and NMC-ref samples display observable transitions in XRD, the 2theta shifts in (003) peaks are more restrained for the NMC-TPA-Ti sample. As illustrated in Figure 12, the maximum change in the (003) peak is 1.2 and 1.4 degrees for NMC-TPA-Ti and NMC-ref, respectively. The lesser reduction in the (003) peak shift for NMC-TPA-Ti is primarily attributed to a lower anisotropic lattice contraction at high cut-off voltages, as both the coated and uncoated samples exhibit a similar amount of lattice change at low cut-off voltages. This can be ascribed to the presence of the protective coating, which effectively controls the structural changes at the high cut-off voltage and regulates anisotropic lattice contraction,[64] in line with expectations derived from dilatometry. This observation is consistent with the results presented in Figure 5b, where it is evident that the NMC-TPA-Ti sample demonstrates higher capacity during cycling compared to the uncoated sample, with a reduced occurrence of detrimental effects.

Recently, a study conducted by Bunyanidhi et al., focusing on the effect of garnet coating on the NMC811 lattice structure, indicated that the (003) reflection exhibits a discontinuity during initial Li deintercalation. This discontinuity suggests that the lithium (de)intercalation in coated NMC811 occurs at a slower pace due to the formation of a secondary phase on the surface, which acts as a Li-ion storage during cycling.[65] However, our results demonstrate that both the NMC-ref and NMC-TPA-Ti samples, as shown in Figure 12a,b, exhibit a gradual Li (de)intercalation mechanism while no secondary phase is detected.

In summary, our opernado XRD analysis of the NMC811 electrode, complementing the dilatometry results, provides valuable insights into the (de)lithiation-induced lattice changes. The TPA-Ti coating effectively controls *c*-axis contraction and restrains volume changes within the electrode, contributing to enhanced cycling stability. This is consistent with the observed suppression of mechanical deformations and reduced undesired volume change in the electrode observed by dilatometry.

Apparently, the nanoscale TPA-Ti coating functions as a protective layer that controls volume changes and the NMC811 particles breathing during cell cycling as observed both in macroscopic and atomic scales. The controlled anisotropic lattice change enhances stability and thus provides higher capacity retention for the cell by facilitating the active material reversible phase changes and mitigating parasitic reactions with the electrolyte within the active material interior. This reduced degradation is the reason behind the higher discharge capacity observed in Figure 5c. These results highlight the significance of coatings in managing structural dynamics and optimizing the performance of composite electrodes.

3. Battery Failure Test

Battery failure testing plays a crucial role in assessing the performance, safety, and durability of battery materials. Specifically, in the case of NMC811 materials, understanding their stability properties is of paramount importance. In this section, battery failure tests on both NMC-ref and NMC-TPA-Ti are conducted to evaluate their thermal and voltage stability. Through these rigorous tests, insight into their behavior is gained under adverse conditions and the potential of the coating in enhancing the thermal and structural stability of NMC811 electrodes at a wider operation range is identified.

Figure 13a illustrates the charge–discharge profiles of the NMC-ref and NMC-TPA-Ti electrodes cycled at 1 C within a voltage range of 3.0–4.6 V. The higher voltage range cycling results in a higher discharge capacity for both samples in the first cycle, with values of 188 and 190 mAh g^{-1} compared to 182 and 185 mAh g^{-1} for the 4.4 V cut-off voltage (Figure 5). However, prolonged cycling reveals significant capacity fades and larger polarization in the NMC-ref 4.6 V-cycled electrode, as shown in Figure 13a. After 100 cycles, the NMC-ref electrode retains 88% of its initial capacity at the 4.4 V operation, while the discharge capacity under 4.6 V voltage cycling decreases to 77%. In contrast, NMC-TPA-Ti experiences less capacity fade at the higher voltage range, with only a 7% decrease compared to the 13% capacity loss observed in NMC-ref.

Liu et al.[66] conducted a comprehensive analysis of a Ni-rich NMC811 electrode to investigate its degradation mechanism during high-voltage cycling. Their study revealed that high-voltage cycling leads to the accumulation of internal resistance in the cell, resulting in faster capacity loss, surface degradation of the cathode, and hindered electrochemical performance, especially compared to moderate-voltage cycling conditions. Additionally, they observed significant changes in the surface morphology of the NMC811 cathode cycled at 4.6 V, indicating the presence of a CEI layer which is formed due to side reactions between the electrode and electrolyte at high operating voltages. Another factor contributing to surface degradation is the generation of microcracks, attributed to the anisotropic lattice volume change during charge/discharge cycling. These microcracks can create new sites for electrolyte reactions and contribute to the growth of the CEI layer. Building upon these findings, our results further support the superior performance of NMC-TPA-Ti by exhibiting better resilience, as more than 90% of its initial capacity remains after 100 cycles in the high-voltage window.

To provide additional insight, high-voltage and low-voltage dilatometry results are compared for the NMC-TPA-Ti electrode. As shown in Figure 13b, the electrode height change remains consistent across different voltage windows for the coated electrode. However, in the higher voltage window, a higher capacity can be achieved, which aligns with the cycling results. This suggests that for NMC-TPA-Ti, the volume change remains controlled even at the wider voltage range due to the presence of the coating, which effectively manages volume fluctuations without impeding Li-ion intercalation. Overall, these findings highlight the potential of the TPA-Ti coating in enhancing the durability and stability of NMC811 electrodes during high-voltage cycling.

In recent studies, the thermal stability of Ni-rich NMC811 electrodes has emerged as a critical concern. The side reactions between the cathodes and electrolytes can generate substantial heat, leading to potentially catastrophic accidents during thermal abuse. To evaluate the thermal stability of NMC-TPA-Ti, long-term cycling experiments in full-cell configurations were employed using graphite as the anode material.

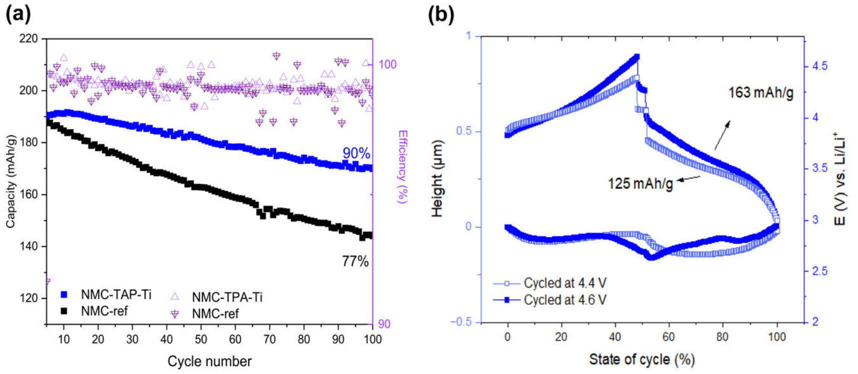

Figure 13. a) Long-term cyclability (charged and discharged at 1 C) of NMC-ref and NMC- TPA-Ti in the voltage range of 3.0–4.6 V in the half-cell configuration. b) Total height change behavior of the NMC- TPA-Ti electrodes during the initial cycle at different voltage windows of 3.0–4.4 and 3.0–4.6 V in the half-cell configuration.

This choice of full cells avoids the negative effects on cycling stability associated with lithium metal anode reactions with carbonate-based electrolytes at high temperatures.[67] In addition, a cut-off voltage of 4.3 V was chosen as a reasonable compromise between achievable capacity and cycling stability.

Consistent with the half-cell data, the NMC-TPA-Ti electrode exhibits excellent stability during cycling up to 4.3 V. Its capacity only slightly declines from the initial value of 180–170 mAh g^{-1} after 100 cycles. In contrast, the NMC-ref electrode shows a faster capacity decline, decreasing from 179 to 140 mAh g^{-1} over 100 cycles. Comparing these results with parallel tests conducted at lower temperatures (Figure 8), all the cells initially exhibit higher capacity, which can be attributed to enhanced reaction kinetics at higher temperatures.

Jalkanen et al.[68] have previously investigated the influence of temperature on battery performance and degradation, highlighting that higher cycling temperatures can improve overall performance by enhancing reaction kinetics. The enhancement in both capacity and reaction kinetics is believed to result from the expanded active surface area of the electrode. This increase in surface area may be attributed to the cracking of positive electrode active material particles, resulting in accelerated degradation processes. Those processes encompass heightened anisotropic volume changes, CEI growth, transitional metal dissolution, and subsequent capacity decay. To confirm these observations, dilatometry tests were conducted at elevated temperatures to investigate the temperature effect on electrode thickness changes. The results, presented in **Figure** 14b,c, clearly demonstrate that the higher temperatures of 40 °C promote capacity increase, which aligns with the cycling results. Although both the NMC-ref and NMC-TPA-Ti electrodes exhibit electrode thickness change at the elevated temperature, the irreversible height change is significantly lower for the latter. This is attributed to the positive effect of the flexible coating, which enhances the structural stability of NMC811 also at elevated temperatures, resulting in remarkable capacity retention (90%) and stability even under high-temperature conditions. Furthermore, the potential negative impact of transition metal dissolution and crossover into the anode side was also investigated. EDS mapping results of the negative electrodes cycled at the elevated temperature reveal a clear crossover of Ni from NMC-ref to the graphite anode, as shown in Figure S10, Supporting Information. In contrast, no Ni can be detected in the graphite cycled with the NMC-TPA-Ti electrode, indicating the ability of TPA-Ti to promote the active material decomposition and transition metal dissolution.[69,70] These findings confirm the effective suppression of harmful side reactions between NMC811 and the electrolyte, as well as the reduction in transition metal dissolution from the active material, resulting in improved electrochemical performance.[71]

To further explore the thermal tolerance of the samples, differential scanning calorimetry (DSC) was conducted. The results are shown in Figure S12, Supporting Information. The thermal reactivity of NMC-TPA-Ti is found to initiate at a higher temperature compared to the uncoated NMC samples, with the main exothermic peak occurring at 227 °C, whereas the exothermic peak associated with NMC811 surface thermal degradation starts at a lower temperature of 222 °C. The thermogravimetric analysis (TGA) analysis reveals lower mass loss for the coated NMC compared to the uncoated sample, confirming the improved thermal stability provided by the ALD-MLD coating.[72]

Overall, battery failure testing conducted on both the NMC-ref and NMC-TPA-Ti materials demonstrates the superior thermal and voltage

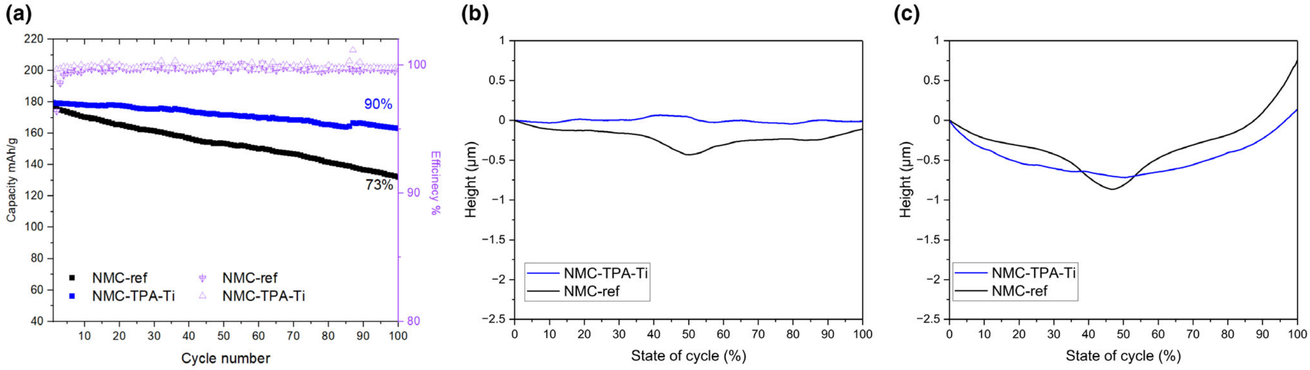

Figure 14. a) Long-term cyclability (charged and discharged at 1 C) in the voltage range of 2.9–4.3 V versus graphite at 40 °C and, total height change behavior during the initial cycle at b) 20 °C (room temperature) and c) 40 °C, in the half-cell configuration at 0.1 C.

stability of the coated NMC811 electrode. The artificial CEI acts as a protective barrier, improving thermal and structural stability. This enhances the overall stability of the battery, reduces the risk of thermal-induced degradation and safety hazards, and helps to maintain stable voltage levels during charge and discharge cycles. These results highlight the importance of surface coatings for high-temperature operations. The TPA-Ti coated NMC811 electrode presented in this study demonstrates the practicality of next-generation high-energy density Li-ion batteries, with excellent cycling stability.

4. Conclusion

In this study, we investigate the potential of TiO_2-titanium terephthalate (TPA-Ti) as a novel nanoscale coating material for NMC811 electrodes using ALD and MLD techniques. Our objective is to evaluate its impact on the electrochemical performance and structural stability of NMC811 electrodes in both half- and full-cell configurations. Various characterization methods were employed to confirm the presence of the TPA-Ti coatings. The electrochemical results show significant improvements in the performance of the NMC811 electrodes with the TPA-Ti coating. Enhanced capacity retention is observed, with the NMC-TPA-Ti electrodes retaining 86% of their initial capacity after 500 cycles, compared to 56% for the uncoated NMC-ref electrodes in the full-cell configuration. Through EIS and CV analysis, thicker CEI growth and irreversible transition in the NMC-ref electrodes are identified to contribute to poor cycling stability in half-cells. In contrast, the TPA-Ti-coated electrodes exhibit reduced crack formation, indicating enhanced structural stability, resistance against degradation, and improved stability. Operando dilatometry measurements further support the controlled structural evolution and mechanical integrity provided by the coatings, even under elevated temperatures or higher cut-off voltages. These findings underscore the crucial role of the TPA-Ti coating in maintaining the mechanical integrity of the NMC811 electrode and stabilizing the electrode-electrolyte interface. In addition, this research opens up new opportunities for the development of ALD-MLD coatings, leading to enhanced overall performance and reliability of lithium-ion batteries.

5. Experimental Section

Electrode preparation: The synthesis of the NMC811 electrode active material involved a solid-state reaction. Specifically, $Ni_{0.8}Mn_{0.1}Co_{0.1}(OH)_2$ (0.06 mol, Umicore Finland Oy) and LiOH (0.06 mol, Sigma–Aldrich, 98%) were combined and calcinated at 800 °C in a tube furnace (Nabertherm) for 12 h, with a controlled heating rate of 3 °C min^{-1}, under a pure oxygen atmosphere. After the sintering process, the resulting powder was carefully ground to eliminate any agglomerates, ensuring a homogeneous and fine-grained material. To prepare the electrodes, a mixture comprising 93 wt% NMC811, 3 wt% carbon black (Timcal Super C65), and 4 wt% polyvinylidene fluoride (PVDF, Solvay, Solef 5130) dissolved in N-methyl-2-pyrrolidone (NMP, Alfa Aesar) was employed. The mixture was thoroughly blended using a dispergator (Dispermat, VMA-Getzmann GMBH-D-51580 Reichshof) at 500 rpm and then coated on a 20 Âμm thick aluminum foil (MTI). The laminated electrodes were dried in a fume hood overnight and subsequently underwent a drying process in an oven at 80 °C for 4 h, promoting the removal of any residual solvent. To achieve the desired electrode configurations, the prepared electrodes were cut into discs with diameters of 18, 14, and 10 mm for the three-electrode cell, coin cell, and dilatometry cell setups, respectively. These discs were then calendared at room temperature under a pressure of 3250 kg cm^{-2}. The electrodes had a loading of 7.5–9.0 mg cm^{-2}, corresponding to approximately 1 mAh cm^{-2} based on the 200 mAh g^{-1} specific capacity of NMC811. The prepared electrodes were dried in a vacuum oven for 12 h at 80 °C and subsequently transferred to an argon-filled glovebox (Jacomex, with oxygen and water levels below 1 ppm) before assembly.

Electrode coating: ALD-MLD (TiO_2-titanium terephthalate:TPA-Ti) coating was deposited on prefabricated NMC811 laminates with a commercial flow-type hot-wall ASM F-120 ALD reactor at 200 °C and below 3 mbar pressure. The films were deposited using titanium tetraisopropoxide (TTIP, Aldrich 97% $Ti[OCH(CH_3)_2]_4$), terephthalic acid (TPA, Aldrich 98% C_6H_3-1,4-$(CO_2H)_2$), and water as precursors. To ensure a sufficient vapor supply for adequate precursor exposure, TTIP and TPA were evaporated inside the reactor using open glass boats at temperatures of 40 and 190 °C, respectively. Nitrogen (99.999%) was employed as both a precursor carrier and purge gas. The TPA-Ti layer was deposited using five supercycles while each supercycle consisted of 12 binary cycles of Ti-water resulting in TiO_2, and one binary cycle of Ti-TPA (TPA/Ti = 1/12). This process resulted in a final coating thickness of approximately 8 nm. A long N_2 purging period was implemented to separate the TTIP precursor and TPA. The pulse/purge times for TTIP and TPA were 2/4s and 10/30s, respectively, while the water pulse/purge for TiO_2 component of the film was 1/6s. As a step before coating the electrodes, initial depositions were carried out on Si wafers measuring 1 cm × 1 cm to optimize the coating thickness. The growth per cycle (GPC) of Ti-TPA was around 1.2 nm on the Si wafer. To differentiate these coated NMC811 electrodes, they are named NMC-TPA-Ti. Accordingly, the bare (uncoated) NMC811 electrodes are labeled as NMC-ref.

Structural characterization: To evaluate the growth per cycle (GPC) of the TPA-Ti coatings deposited on the Si substrate, X-ray reflectivity (XRR) measurements were performed using a PANalytical X'Pert Pro Alpha 1 MPD instrument. The XRR analysis utilized Cu Kα1 radiation at 40 kV and 45 mA. The obtained XRR data were analyzed and fitted using the PANalytical X'Pert Reflectivity program to determine the film thickness and GPC of the coating (Figure S1, Supporting Information). Further details regarding the XRR characterization and GPC calculation can be found in our previous work.[22] In addition, a range of structural and chemical characterization techniques were employed to confirm the successful deposition of TPA-Ti and investigate its impact on the NMC811 electrode. The morphological characteristics and element distribution of the coated and uncoated NMC811 electrodes were analyzed using scanning electron microscopy (SEM) with JEOL JIB-4700F instruments, coupled with energy-dispersive X-ray spectroscopy (EDS). The SEM was operated at 10 kV, while the EDS analysis was performed at 20 kV. To investigate the structural and elemental changes, as well as coating thickness on the surface of the NMC811 electrodes, focused-ion beam (FIB) cutting and transmission electron microscopy (TEM) techniques were employed. FIB processing was conducted using a JEOL JIB-4700F instrument, utilizing a high-current density Ga-ion beam for fast ion milling and specimen processing. The FIB method allowed for the cross-sectional cutting of the coated NMC811 electrodes and the preparation of a lamella for TEM analysis. Prior to analysis, a protective Pt layer was deposited on the sample surface to prevent damage during preparation. The cross-sectional structure of the prepared samples was examined using TEM-EDS with a JEOL JEM-2200FS double aberration-corrected microscope equipped with a 200 kV field-emission gun (FEG) and an X-ray EDS detector. Fourier transform infrared spectroscopy (FTIR) was employed to analyze the chemical bonding of the deposited TPA-Ti film, specifically on Si-coated substrates and NMC811 electrodes, using a Bruker alpha II instrument. X-ray photoelectron spectroscopy (XPS) using an Axis Ultra instrument from Kratos was used to investigate the surface composition of the samples. High-resolution data were collected with a 0.1 eV energy step and a pass energy of 40 eV. The XPS spectra were processed using CasaXPS software and calibrated using the C 1s (BE = 284.8 eV) photoelectron lines. Additionally, delithiated cathodes were subjected to differential scanning calorimetry and thermogravimetric analysis (DSC-TGA) using a Netzsch DSC 204 F1 Phoenix device. The measurements were conducted under a nitrogen atmosphere, with a heating rate of 10 °C min^{-1}, in the temperature range of room temperature to 500 °C.

Electrochemical investigations: Electrochemical investigations were conducted to compare the properties of coated and uncoated NMC811 samples. Coin cells CR-2016 (Hohsen) were assembled in an argon-filled glove box with either NMC-ref or the coated electrode. Half-cell assembly involved using lithium metal foil discs (19 mm diameter, 0.74 mm thickness, Goodfellow) as the anode and fiberglass discs (GF/A 0.26 mm, Whatman) as the separator. The electrolyte used for half-cells was a solution of 1 M $LiPF_6$ in ethylene carbonate

(EC)/ethylmethyl carbonate (EMC) (1:1 mixture by weight, Sigma–Aldrich). After assembly, the cells were allowed to rest for 24 h before conducting electrochemical studies at room temperature. Galvanostatic charge–discharge experiments were performed using a Land battery test system (V7), and rate capability measurements were conducted at various C-rates (1 C = 200 mA g^{-1}). Additionally, long-term cyclability tests were carried out by cycling the samples at 1 C using a constant current-constant voltage (CC-CV) and constant current (CC) mode, within the voltage range of 3.0–4.4 V and 3.0–4.6 V versus Li/Li^+, respectively. To ensure result reproducibility, at least two parallel samples were measured. For full-cell assembly, both coated and uncoated NMC811 samples were used in coin cells. The assembly included graphite (MTI) as the negative electrode and a ceramic-coated polymer film (Gelon) as the separator. The graphite electrode size was 14 mm, and the separator size was 19 mm. The electrolyte employed was 1 M $LiPF_6$ in a 25:70:5 ethylene carbonate (EC)/diethylene carbonate/propylene carbonate solution with 1 mol% vinylene carbonate (E-Lyte). After assembly, the cells were allowed to rest for 24 h and then formatted by cycling at 0.1 C (three times) before conducting galvanostatic charge–discharge experiments at room temperature and 40 °C. Dilatometry analysis was performed using an ECD-3-nano (EL-CELL) dilatometer to investigate the operando volume change of the NMC811 and TPA-Ti-coated NMC811 electrodes with different coating thicknesses (10 mm diameter). The setup involved using lithium foil as a counter electrode and a glass frit separator to mitigate the height change effect of the counter electrode. Dilatometry measurements were conducted at different voltage windows between 3.0 and 4.4 V or 3.0 and 4.6 V versus Li/Li^+. The measurements were also done inside a climatic chamber (VC3 4018) at fixed temperatures of 20 and 40 °C. Cyclic voltammetry (CV) and electrochemical impedance spectroscopy (EIS) measurements were performed on a three-electrode cell using a Biologic potentiostat (MPG-205). CV measurements were taken after the initial formation cycles at 0.02 mV s^{-1} and the potential sweep range was set between 3.0 and 4.4 V versus Li/Li^+ at scan rates of 0.02, 0.1, 0.2, and 0.5 mV s^{-1}. The impedance spectra were obtained at 50% state of charge (SOC) of the cell, covering a frequency range from 100 kHz to 10 mHz. EIS measurements were conducted after the formation and 50th cycle at a rate of 1 C. The resulting spectra were analyzed and fitted using Zview software. Operando XRD measurements were performed to monitor the lattice change during the charge–discharge process. The ECC-Opto-Std cell was equipped with a Be window while a mylar film was used to prevent Be window oxidation at high operating voltages. The cell was operated at a C-rate of around 0.1 C (1 C = 200 mAh g^{-1}) for all electrodes using an Ivium Vertex Potentiostat. XRD patterns were collected simultaneously using a PANalytical X'Pert Pro MPD Alpha-1 diffractometer with Cu Kα1-radiation, having a wavelength of 0.15406 nm (operating at 45 kV and 40 mA). A compromise was achieved between intensity and time resolution by collecting patterns over a relatively small angular range of 17–47.5° with a collection time of 17 min per pattern. About 60 XRD patterns can be collected during the complete charge–discharge progress. Rietveld refinement was carried out by GSAS-II software. Size, sample displacement parameter, and the background profile function were refined at the beginning for the first pattern and then applied to all patterns. The coated and uncoated NMC811 positive electrodes studied here are isostructural with a layered structure that belongs to the space group R-3m. The *c*-lattice parameter was mainly determined from the peak fitting of (003) because the (006) peak has substantial noise in high delithiated patterns.

Post-mortem characterization: The cycled NMC-ref and NMC-TPA-Ti electrodes were carefully retrieved from disassembled cells in the glove box and dried overnight prior to the post-mortem structural characterization. To gain insights into the internal structure of the electrodes, holotomography analysis was employed. Tomographic scans were conducted on the NMC-ref and TPA-Ti-NMC electrodes after the formation cycle, as well as after 20 and 50 aging cycles, at the ESRF ID16B beamline. The tomographic scans were carried out using an incident X-ray beam with an energy of 29.6 keV and a flux of 1.42×10^{12} photons per second. Two scans were performed at different sample-detector propagation distances. Each scan involved the recording of 2515 projections, along with 21 reference and dark images, using a PCO edge 5.5 camera (2560×2160 $pixels^2$). The sample was rotated 360° during the scan, with an exposure time of 25 ms per step. The entire acquisition process took approximately 15 min per holotomography scan. The voxel size was set at 25 nm, resulting in fields of view of 64×54 μm^2. To reconstruct the images, a filtered back projection reconstruction method was employed using the PyHST2 software provided by ESRF.[53,73]

Acknowledgements

This work made use of the Aalto University Otanano-Nanomicroscopy Center and RAMI infrastructures. Financial support from Business Finland NextGenBat [grant number 211849] is greatly acknowledged. The tomography experiment was performed at the beamline ID16B of the European Synchrotron Radiation Facility (ESRF), Grenoble, France, in the frame of proposal CH-6644. The patent titled "Stabilized Positive Electrode Material to Enable High Energy and Power Density Lithium-Ion Batteries" (IPD3173) is pertinent to this manuscript. It was filed by Zahra Ahaliabadeh and Tanja Kallio, and the patent rights are held by Aalto University.

Conflict of Interest

The authors declare no conflict of interest.

Supporting Information

Supporting Information is available from the Wiley Online Library or from the author.

Keywords

degradation mechanisms, electrolyte decomposition, hybrid coatings, lithium-ion battery, lithium-ion kinetics, molecular layer deposition, NMC811

Received: January 7, 2024
Revised: February 1, 2024
Published online: February 15, 2024

---

[1] T.-P. Gao, K. W. Wong, K. Y. Fung, W. Zhang, K. M. Ng, *Electrochim. Acta* **2018**, *288*, 153.

[2] W.-W. Li, X.-J. Zhang, J.-J. Si, J. Yang, X.-Y. Sun, *Rare Metals* **2020**, DOI: 10.1007/s12598-020-01483-5

[3] J. Ahn, E. K. Jang, S. Yoon, S.-J. Lee, S.-J. Sung, D.-H. Kim, K. Y. Cho, *Appl. Surf. Sci.* **2019**, *484*, 701.

[4] H. Wu, X. Zhou, C. Yang, D. Xu, Y.-H. Zhu, T. Zhou, S. Xin, Y. You, *ACS Appl. Mater. Interfaces* **2023**, *15*, 18828.

[5] W. Zhu, X. Huang, T. Liu, Z. Xie, Y. Wang, K. Tian, L. Bu, H. Wang, L. Gao, J. Zhao, *Coatings* **2019**, *9*, 92.

[6] O. Tiurin, Y. Ein-Eli, *Adv. Mater. Interfaces* **2019**, *6*, 1901455.

[7] M. J. Herzog, D. Esken, J. Janek, *Batter. Supercaps* **2021**, *4*, 1003.

[8] M. J. Herzog, N. Gauquelin, D. Esken, J. Verbeeck, J. Janek, *ACS Appl. Energy Mater.* **2021**, *4*, 8832.

[9] T. Li, X.-Z. Yuan, L. Zhang, D. Song, K. Shi, C. Bock, *Electrochem. Energy Rev.* **2020**, *3*, 43.

[10] M. Wang, Y. Gong, Y. Gu, Y. Chen, L. Chen, H. Shi, *Ceram. Int.* **2019**, *45*, 3177.

[11] J. Hu, L. Li, E. Hu, S. Chae, H. Jia, T. Liu, B. Wu, Y. Bi, K. Amine, C. Wang, J. Zhang, J. Tao, J. Xiao, *Nano Energy* **2021**, *79*, 105420.

[12] T. Wang, Y. Hua, Z. Xu, J. S. Yu, *Small* **2022**, *18*, 2102250.

[13] M. H. Aboonasr Shiraz, E. Rehl, H. Kazemian, J. Liu, *Nano* **2021**, *11*, 1976.

[14] L. Momtazi, H. H. Sønsteby, D. Dartt, J. R. Eidet, O. Nilsen, *RSC Adv.* **2017**, *7*, 20900.

[15] A. Philip, J.-P. Niemela, G. C. Tewari, B. Putz, T. E. J. Edwards, M. Itoh, I. Utke, M. Karppinen, *ACS Appl. Mater. Interfaces* **2020**, *12*, 21912.

[16] Y. Chen, W. Zhao, Q. Zhang, G. Yang, J. Zheng, W. Tang, Q. Xu, C. Lai, J. Yang, C. Peng, *Adv. Funct. Mater.* **2020**, *30*, 2000396.

[17] D. M. Piper, Y. Lee, S.-B. Son, T. Evans, F. Lin, D. Nordlund, X. Xiao, S. M. George, S.-H. Lee, C. Ban, *Nano Energy* **2016**, *22*, 202.

[18] S. S. Vandenbroucke, L. Henderick, L. L. De Taeye, J. Li, K. Jans, P. M. Vereecken, J. Dendooven, C. Detavernier, *ACS Appl. Mater. Interfaces* **2022**, *14*, 24903.

[19] K. Beltrop, S. Klein, R. Nölle, A. Wilken, J. J. Lee, T. K. J. Köster, J. Reiter, L. Tao, C. Liang, M. Winter, X. Qi, T. Placke, *Chem. Mater.* **2018**, *30*, 2726.

[20] V. Vijayakumar, M. Ghosh, K. Asokan, S. B. Sukumaran, S. Kurungot, J. Mindemark, D. Brandell, M. Winter, J. R. Nair, *Adv. Energy Mater.* **2023**, *13*, 2203326.

[21] G. Park, H. Park, W. Seol, S. Suh, J. Kim, J. Y. Jo, H.-J. Kim, *Electrochim. Acta* **2022**, *409*, 139984.

[22] Z. Ahaliabadeh, V. Miikkulainen, M. Mantymaki, S. Mousavihashemi, J. Lahtinen, Y. Lide, H. Jiang, K. Mizohata, T. Kankaanpaa, T. Kallio, *ACS Appl. Mater. Interfaces* **2021**, *13*, 42773.

[23] P. Teichert, H. Jahnke, E. Figgemeier, *J. Electrochem. Soc.* **2021**, *168*, 90532.

[24] J. Liang, S. Hwang, S. Li, J. Luo, Y. Sun, Y. Zhao, Q. Sun, W. Li, M. Li, M. N. Banis, X. Li, R. Li, L. Zhang, S. Zhao, S. Lu, H. Huang, D. Su, X. Sun, *Nano Energy* **2020**, *78*, 105107.

[25] K. Marker, P. J. Reeves, C. Xu, K. J. Griffith, C. P. Grey, *Chem. Mater.* **2019**, *31*, 2545.

[26] R. Ghiyasi, G. C. Tewari, M. Karppinen, *J. Phys. Chem. C* **2020**, *124*, 13765.

[27] J. Heiska, M. Nisula, E.-L. Rautama, A. J. Karttunen, M. Karppinen, *Dalton Trans.* **2020**, *49*, 1591.

[28] L. Seidl, R. Grissa, L. Zhang, S. Trabesinger, C. Battaglia, *Adv. Mater. Interfaces* **2022**, *9*, 2100704.

[29] M. M. Sanad, N. K. Meselhy, H. A. El-Boraey, A. Toghan, *J. Mater. Res. Technol.* **2023**, *23*, 1528.

[30] X. Qu, H. Huang, T. Wan, L. Hu, Z. Yu, Y. Liu, A. Dou, Y. Zhou, M. Su, X. Peng, H. H. Wu, T. Wu, D. Chu, *Nano Energy* **2022**, *91*, 106665.

[31] X. Xiao, X. Deng, Y. Tian, S. Tao, Z. Song, W. Deng, H. Hou, G. Zou, X. Ji, *Nano Energy* **2022**, *103*, 107797.

[32] W. Li, X. Liu, Q. Xie, Y. You, M. Chi, A. Manthiram, *Chem. Mater.* **2020**, *32*, 7796.

[33] C. Ye, W. Tu, L. Yin, Q. Zheng, C. Wang, Y. Zhong, Y. Zhang, Q. Huang, K. Xu, W. Li, *J. Mater. Chem. A* **2018**, *6*, 17642.

[34] Y. Zhang, T. Kang, X. Han, W. Yang, W. Gong, K. Li, Y. Guo, *Nano Energy* **2023**, *111*, 108433.

[35] Z. Zhang, C. Yan, C. Liu, X. Ye, X. Yuan, H. Li, *Nanotechnology* **2022**, *33*, 485705.

[36] Y. Xia, J. Zheng, C. Wang, M. Gu, *Nano Energy* **2018**, *49*, 434.

[37] N. Phattharasupakun, P. Bunyanidhi, P. Chiochan, N. Chanlek, M. Sawangphruk, *Electrochem. Commun.* **2022**, *139*, 107309.

[38] B. P. Thapaliya, S. Misra, S.-Z. Yang, C. J. Jafta, H. M. Meyer III, P. Bagri, R. R. Unocic, C. A. Bridges, S. Dai, *Adv. Mater. Interfaces* **2022**, *9*, 2200035.

[39] T. Kim, *Mater. Today Sustain.* **2023**, *21*, 100326.

[40] Y. Gao, J. Park, X. Liang, *ACS Appl. Energy Mater.* **2020**, *3*, 8978.

[41] S. H. Akella, S. Taragin, Y. Wang, H. Aviv, A. C. Kozen, M. Zysler, L. Wang, D. Sharon, S. B. Lee, M. Noked, *ACS Appl. Mater. Interfaces* **2021**, *13*, 61733.

[42] Y. Zhai, W. Yang, D. Ning, J. Yang, L. Sun, G. Schuck, G. Schumacher, X. Liu, *J. Mater. Chem. A* **2020**, *8*, 5234.

[43] Z. Ahaliabadeh, X. Kong, E. Fedorovskaya, T. Kallio, *J. Power Sources* **2022**, *540*, 231633.

[44] B. Nan, L. Chen, N. D. Rodrigo, O. Borodin, N. Piao, J. Xia, T. Pollard, S. Hou, J. Zhang, X. Ji, J. Xu, X. Zhang, L. Ma, X. He, S. Liu, H. Wan, E. Hu, W. Zhang, K. Xu, X. Q. Yang, B. Lucht, C. Wang, *Angew. Chem. Int. Ed.* **2022**, *61*, e202205967.

[45] U. Nisar, N. Muralidharan, R. Essehli, R. Amin, I. Belharouak, *Energy Storage Mater.* **2021**, 38, 309.

[46] A. K. Haridas, Q. A. Nguyen, T. Terlier, R. Blaser, S. L. Biswal, *ACS Appl. Mater. Interfaces* **2021**, *13*, 2662.

[47] N. D. Phillip, A. S. Westover, C. Daniel, G. M. Veith, *ACS Appl. Energy Mater.* **2020**, *3*, 1768.

[48] H. Gao, J. Cai, G.-L. Xu, L. Li, Y. Ren, X. Meng, K. Amine, Z. Chen, *Chem. Mater.* **2019**, *31*, 2723.

[49] X. Liu, T. Liu, R. Wang, Z. Cai, W. Wang, Y. Yuan, R. Shahbazian-Yassar, X. Li, S. Wang, E. Hu, X.-Q. Yang, Y. Xiao, K. Amine, J. Lu, Y. Sun, *ACS Energy Lett.* **2020**, *6*, 320.

[50] D. Aurbach, E. Markevich, G. Salitra, *J. Am. Chem. Soc.* **2021**, *143*, 21161.

[51] J. Guo, Y. Li, J. Meng, K. Pedersen, L. Gurevich, D.-I. Stroe, *J. Energy Chem.* **2022**, *74*, 34.

[52] H. Yu, Y. Gao, X. Liang, *J. Electrochem. Soc.* **2019**, *166*, A2021.

[53] Z. Ahaliabadeh, M. Colalongo, V. Miikkulainen, *Understanding the Stabilizing Effects of Nanoscale Coatings on Lithium-Ion Battery Positive Electrode Materials (NMC811)*, European Synchrotron Radiation Facility. **2023**.

[54] H. Fathiannasab, A. G. Kashkooli, T. Li, L. Zhu, Z. Chen, *J. Electrochem. Soc.* **2020**, *167*, 100558.

[55] F. Xin, A. Goel, X. Chen, H. Zhou, J. Bai, S. Liu, F. Wang, G. Zhou, M. S. Whittingham, *Chem. Mater.* **2022**, *34*, 7858.

[56] T.-T. Nguyen, J. Villanova, Z. Su, R. Tucoulou, B. Fleutot, B. Delobel, C. Delacourt, A. Demorti'ere, *Adv. Energy Mater.* **2021**, *11*, 2003529.

[57] H. Zhang, X. He, Z. Chen, Y. Yang, H. Xu, L. Wang, X. He, *Adv. Energy Mater.* **2022**, 12, 2202022.

[58] S. Sharifi-Asl, V. Yurkiv, A. Gutierrez, M. Cheng, M. Balasubramanian, F. Mashayek, J. Croy, R. Shahbazian-Yassar, *Nano Lett.* **2019**, *20*, 1208.

[59] T. M. Heenan, A. Wade, C. Tan, J. E. Parker, D. Matras, A. S. Leach, J. B. Robinson, A. Llewellyn, A. Dimitrijevic, R. Jervis, P. D. Quinn, D. J. L. Brett, P. R. Shearing, *Adv. Energy Mater.* **2020**, *10*, 2002655.

[60] F. B. Spingler, S. Kücher, R. Phillips, E. Moyassari, A. Jossen, *J. Electrochem. Soc.* **2021**, *168*, 40515.

[61] S. Mousavihashemi, K. Lahtinen, T. Kallio, *Electrochim. Acta* **2022**, *412*, 140093.

[62] Y. Li, X. Liu, D. Ren, H. Hsu, G.-L. Xu, J. Hou, L. Wang, X. Feng, L. Lu, W. Xu, Y. Ren, R. Li, X. He, K. Amine, M. Ouyang, *Nano Energy* **2020**, *71*, 104643.

[63] Z. Ruff, C. S. Coates, K. Märker, A. Mahadevegowda, C. Xu, M. E. Penrod, C. Ducati, C. P. Grey, *Chem. Mater.* **2023**, 35, 4987.

[64] W. Hua, B. Schwarz, R. Azmi, M. Müller, M. S. D. Darma, M. Knapp, A. Senyshyn, M. Heere, A. Missyul, L. Simonelli, J. R. Binder, S. Indris, H. Ehrenberg, *Nano Energy* **2020**, *78*, 105231.

[65] P. Bunyanidhi, N. Phattharasupakun, C. Tomon, S. Duangdangchote, P. Kidkhunthod, M. Sawangphruk, *J. Power Sources* **2022**, *549*, 232043.

[66] H. Liu, Z. Xie, W. Qu, E. Dy, S. Niketic, S. Brueckner, K. Tsay, E. Fuller, C. Bock, N. Zaker, G. A. Botton, *Small* **2022**, *18*, 2200627.

[67] B. Jiang, H. Xu, X. Cheng, J. Li, H. Wang, Y. Liu, *ChemElectroChem* **2022**, 9, e202101251.

[68] K. Jalkanen, J. Karppinen, L. Skogström, T. Laurila, M. Nisula, K. Vuorilehto, *Appl. Energy* **2015**, *154*, 160.

[69] Z. Ruff, C. Xu, C. P. Grey, *J. Electrochem. Soc.* **2021**, *168*, 60518.

[70] Z. Yang, H. Charalambous, S. E. Trask, A. Montoya, A. Jansen, K. M. Wiaderek, I. Bloom, *J. Power Sources* **2022**, *549*, 232119.

[71] P. J. West, C. D. Quilty, Z. Wang, S. N. Ehrlich, L. Ma, C. Jaye, D. A. Fischer, X. Tong, A. M. Kiss, E. S. Takeuchi, A. C. Marschilok, K. J. Takeuchi, D. C. Bock, *J. Phys. Chem. C* **2023**, *127*, 7054.

[72] A. L. Lipson, B. J. Ross, J. L. Durham, D. Liu, M. LeResche, T. T. Fister, L. Liu, K. Kim, *ACS Appl. Energy Mater.* **2021**, *4*, 1972.

[73] S. L. Burg, A. L. Washington, J. Villanova, A. J. Dennison, D. McLoughlin, O. O. Mykhaylyk, P. Vukusic, W. Furnass, R. A. Jones, A. J. Parnell, J. P. A. Fairclough, *Sci. Data* **2020**, *7*, 163.